Spin-Injection Enhancements in van der Waals Magnetic Tunnel Junctions through Barrier Engineering

Jonathan J. Heath and Marcelo A. Kuroda

Phys. Rev. Applied **16**, L041001 — Published 15 October 2021

DOI: 10.1103/PhysRevApplied.16.L041001

Spin injection enhancements in van der Waals magnetic tunnel junctions through barrier engineering

Jonathan J. Heath and Marcelo A. Kuroda*
Department of Physics, Auburn University, Auburn AL 36849, USA
(Dated: September 8, 2021)

The weak interlayer coupling in two-dimensional materials enables the formation of sharp crystalline magnetic tunnel junctions without the epitaxial constraints found in the bulk. Amid the large number of heterostructures that can be formed using these layered materials, a means to guide the experimental design of systems with enhanced responses is desired. Here we show that meaningful improvements in spin injection are attained by tailoring the tunneling barriers through the choice of the metal electrodes. Owing to the weak coupling between layers, the barrier engineering can be rationalized from properties of bulk components from first principles calculations leading to superior spin injection and magnetoresistance. Analysis of CrI_3 junctions formed with transition metal dichalcogenide electrodes shows that junction conductivities increase by nearly three orders of magnitude with respect to those experimentally demonstrated with graphite leads. Moreover, we find that tunneling magnetoresistance significantly augments with low work function electrodes when carriers are injected near the CrI_3 conduction band edge. The predictive approach employed in this work shows good agreement with detailed quantum transport calculations and can potentially accelerate the design of tunnel junctions based on two-dimensional materials.

Heterostructures formed with two-dimensional (2D) materials are receiving considerable attention as platforms for a variety of novel physical phenomena, which benefit from sharp interfaces, few-atom-thicknesses and the weak van der Waals (vdW) coupling [1, 2]. Recent experimental demonstrations of magnetic tunnel junctions (MTJs) based on few-layer CrX_3 (X = Cl, Br, and I) reported tunneling magneto-resistance (TMR) values ranging between 50-200% for bilayer junctions [3, 4], which can be substantially enlarged in multilayer CrI_3 channels through electrostatic gating [5–8]. Despite the colossal TMR achieved in these devices, the use of graphitic leads in concert with the CrX_3 channel yields low conductivity values ($\lesssim 10^{-7}$ S·μm^{-2} in bilayer junctions [3, 4]) due to graphene's vanishing density of states near the Fermi level. In addition to facilitating read-out, high current densities (in- and out-of-plane) may be exploited as switching mechanisms via spin-orbit torque [9, 10]. Therefore, identifying alternative electrode materials is imperative to meaningfully advance the development of these junctions.

Development of 2D material spintronic devices has spawned a variety of efforts [11]. For instance, theoretical studies have proposed the use of Cu leads in CrI_3 junctions [12], or magnetic transition metal dichalcogenides (TMDs) such as magnetic 1T-VX_2 (X = Se and Te) as lead or channel materials [13–15] as mechanisms to enhance the TMR response. Complementarily, experimental endeavors have also explored changes in the channel or electrodes to form improved junctions based on 2D materials [16–21]. However, the continuously growing family of 2D materials and the absence of epitaxial constraints between layers gives innumerable material combinations, demanding guiding principles for the optimal design of these vdW heterostructures.

Here we exploit barrier engineering to form 2D material heterostructures with increased conductivities and TMR. Design guidelines are based on the physical properties of individual constituents (electrodes and channels) obtained from first principles. In exemplary systems with CrI_3 tunneling barriers and TMD electrodes, we find that TMD electrodes yield conductivities nearly three orders of magnitude larger than those attained with graphite electrodes. More importantly, we anticipate meaningful improvements in TMR using low work function electrodes in CrI_3 (and $CrBr_3$) junctions. We compare the predictions of this approach to more detailed descriptions of tunneling using the non-equilibrium Green's function (NEGF) formalism. We discuss the virtues and limitations of this design scheme that, by prioritizing material candidates using bulk or isolated properties, may foster rapid advancements in the realization of 2D material based tunnel junctions.

Improvements of MTJ characteristics must ensure either an increase in tunneling current or TMR, ideally both. In order to enhance these quantities, two physical parameters of vdW heterostructures are *a priori* key: (*i*) energy dependent tunneling rates of the channel associated to evanescent states and (*ii*) a large density of states (DOS) in the electrodes near the Fermi level. In 2D material heterostructures, such as CrI_3 magnetic insulators and TMD leads, features of individual layers are, to some extent, preserved due to the weak vdW coupling between them. To characterize these features, we perform first principles calculations within the density functional theory (DFT) using the generalized-gradient approximation of the exchange-correlation potential [22], including dispersion forces (vdW-DF-C09) [23–25]. Atomic cores are represented via projector augmented wave (PAW) pseudopotentials [26, 27] using cutoff energies of 50 Ry and

* mkuroda@auburn.edu

500 Ry regarding the Kohn-Sham wave functions and densities, respectively. The Brillouin zone (BZ) is sampled through a 12×12×8 mesh [28] for bulk electrodes and a 12×12×1 for heterostructures, employing the Quantum Espresso software [29, 30].

Here, the effective energy-dependent decay rates in a tunneling barrier are gauged from the complex band structure (CBS) of its bulk form [31, 32]. For a magnetic state m, not only complex wave vectors (κ) vary between spin populations, but also show prominent dependence on the in-plane crystal momentum ($\mathbf{k}_\parallel$) and the energy of the evanescent mode propagating through the channel. Figure 1(a) illustrates the bulk CrI_3 CBS for both FM and AFM magnetic configurations along the Γ-A, M-L, and K-H symmetry lines of the hexagonal crystal. Despite its larger band gap, the FM spin minority (red) population have imaginary wave vectors that are comparable or at times shorter (e.g. Γ-A symmetry path near the CrI_3 mid-gap) than the FM spin majority (blue) or the AFM cases. This counter-intuitive feature tampers magnetic state differentiation based on spin currents as discussed below.

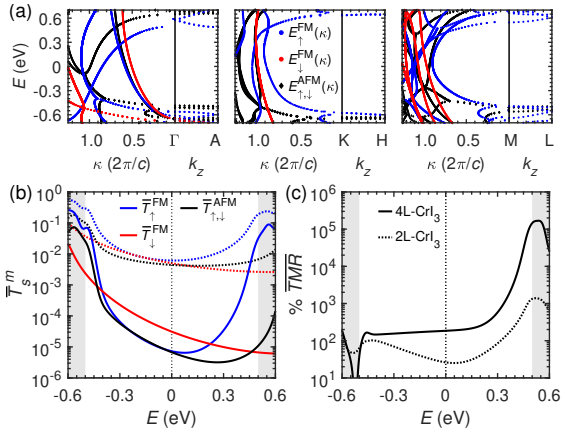

FIG. 1. (a) CBS for bulk CrI_3 along different symmetry lines (from left to right): Γ-A, K-H, and M-L. Blue (red) lines represent majority (minority) evanescent states produced in the FM configuration while gray lines correspond to states in the AFM configuration. (b) Approximate transmission probabilities $\overline{T}_s^m(E)$ and (c) corresponding $\overline{\text{TMR}}$ results obtained from CBS for CrI_3 channels with bilayer (2L) and tetralayer (4L) thicknesses. Energies are referenced to the FM CrI_3 spin majority mid gap and shaded areas denote the location of the valence and conduction bands.

Within the Landauer formalism, ballistic conductivity in the magnetic state m is given by $\sigma_m = G_0/A \sum_{s=\uparrow,\downarrow} T_s^m(E)$, where $G_0 = e^2/h \approx 38.7$ μS represents the conductance quantum [33] and A represents the channel's cross-sectional area. The quantity $T_s^m(E)$ denotes the transmission probability corresponding to the spin channel s ($s = \uparrow, \downarrow$) [34, 35]:

$$T_s^m(E) = \frac{A}{(2\pi)^2} \int dE \int_{\text{2D-BZ}} d^2\mathbf{k}_\parallel \sum_{i,j} t_{i,j}^{s,m}(\mathbf{k}_\parallel, E) \frac{df}{dE}, \quad (1)$$

where $t_{i,j}^{s,m}(\mathbf{k}_\parallel, E)$ and $f(E)$ are the transmission of individual modes and the Fermi distribution, respectively. We first estimate the energy dependent transmission $\overline{T}_s^m(E)$ solely using CBS of CrI_3 barriers, assuming that all regions of the BZ contribute equally. This ansatz is based on the uniform coverage of the BZ by the electrode's Fermi surface and is further discussed later. To this end, each mode transmission is computed as

$$\bar{t}_{i,j}^{s,m}(\mathbf{k}_\parallel, E) = \exp[-2\kappa_{s,m}(\mathbf{k}_\parallel, E)\ell], \quad (2)$$

in terms of their complex wave vectors $\kappa_{s,m}(\mathbf{k}_\parallel, E)$. The tunneling barrier thickness $\ell = Nd$ is expressed in terms of the number of layers N and the interlayer distance ($d \approx 6.4$ Å for CrI_3).

Spin-resolved transmission estimates $\overline{T}_s^m(E)$ for bilayer (2L) and tetralayer (4L) CrI_3 channel in the FM and AFM configurations are obtained using Eqs. 1 and 2. As channel thickness increases, transmissions diminish by nearly an order of magnitude per layer for energies within the majority mid gap, where longer complex wavevectors reside. As anticipated from the CBS, at these energy levels, spin majority transmissions in the 4L-CrI_3 FM configuration subside with respect to the minority spin transmissions while remain comparable to transmissions in the AFM configuration (black). Near the band edges, the FM spin majority transmission decays more slowly and becomes significantly different than those in the AFM configuration.

Differentiation in conductivity between magnetic states is quantified by the TMR:

$$\text{TMR} = \frac{|\sigma_{\text{FM}} - \sigma_{\text{AFM}}|}{\sigma_{min}}, \quad (3)$$

where $\sigma_{min} = \min(\sigma_{\text{AFM}}, \sigma_{\text{FM}})$ is the least conductive magnetic configuration. In Fig. 1(c) we present the energy dependent TMR corresponding to 2L- and 4L-thick CrI_3 channels using CBS-derived transmissions $\overline{T}_s^m(E)$, aligning the spin majority valence band edges. Overall, the TMR enhances as channel thickness increases albeit with smaller junction conductivities. More importantly, TMR estimates raise by few orders of magnitude near the conduction band edge (CBE) owing to the smaller decay rates of spin majority carriers at these energy levels (Fig. 1) but drastically shrinks near the valence band edge (VBE). Therefore, low work function electrodes, injecting carriers near the CBE, may significantly improve TMR values in these junctions.

To test these predictions, we consider electrode candidates formed by metallic transition metal dichalcogenides (TMD), which not only belong to one of the most widely studied 2D material families but also adopt various polymorphs (e.g. 1T, 2H, 1T' and pbca) [36, 37]. We then screen the most stable transition metal polymorphs using DFT [38] and compute their work functions ϕ. For these systems, work functions range from ∼4 eV to 7 eV, as illustrated for those with hexagonal lattices (1T and 2H) in Fig. 2(a) and for the remaining (1T' and Pbca) phases

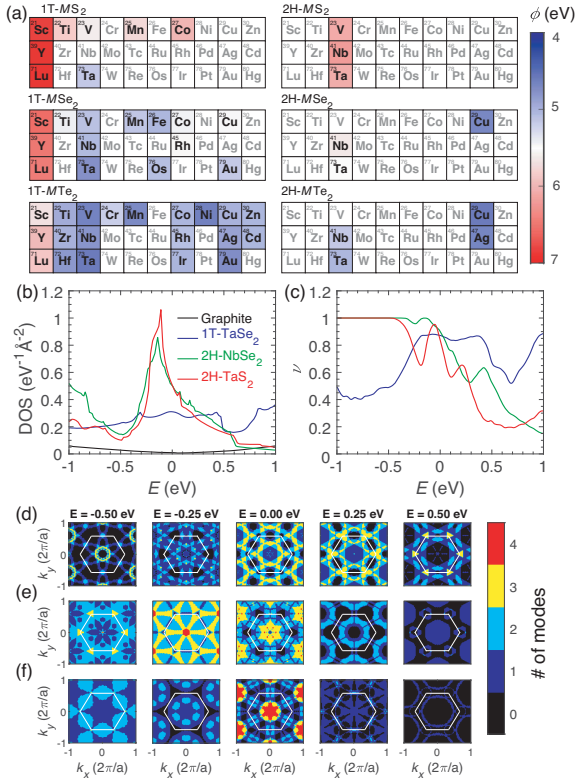

FIG. 2. (a) Colormap of most stable metallic TMD monolayer work functions as obtained from DFT, where transition metals are arranged following their location in the periodic table; each row corresponds to a different chalcogen element: sulfur (top), selenium (middle), and tellurium (bottom); columns denote 1T (left) and 2H (right) phase. (b) DOS for monolayer TMDs: 1T-$TaSe_2$ (blue), 2H-$NbSe_2$ (green), and 2H-TaS_2 (red). For comparison graphene is also shown. (c) 2D-BZ filling factor $\nu(E)$ for TMD bulk electrodes with 2×2 epitaxy. Electron modes of bulk electrodes at various energy levels: (d) 1T-$TaSe_2$, (e) 2H-$NbSe_2$, and (f) 2H-TaS_2. Hexagons denote the 2D BZ edges.

in the Supplemental Information [38]. Subsequently we narrow down the TMD candidates by selecting those realized experimentally [39–43], allowing supercells tractable within DFT with small lateral strain ($\lesssim 3\%$) and offering different band alignments with CrI_3. Considering these criteria, we focus our efforts on 1T-$TaSe_2$ [44] ($\phi = 4.8$ eV), 2H-$NbSe_2$ [39] ($\phi = 5.6$ eV), and 2H-TaS_2 [45] ($\phi = 6.1$ eV) as cases with a low, intermediate and high work function, respectively.

The Fermi level DOS of these TMD electrodes is substantially larger than that of graphene [Fig. 2(b)]. Furthermore, we analyze the distribution of states (modes) within the 2D BZ, accounting for the 2×2 epitaxy used in this work when forming interfaces with CrI_3. We define the filling factor $\nu(E)$ as the fraction of the bulk electrode 2D-BZ which hosts transport modes at a certain energy level as portrayed in Fig. 2. For the chosen TMD electrodes, nearly ideal Fermi level filling factors ($\nu(E_F) \sim 1$) are observed, a key assumption in our CBS estimates (Eq. 2).

Next, we analyze the electronic properties and spin transport in TMD/CrI_3 heterostructures composed of 2L- or 4L-CrI_3 channels. In these model supercells, three TMD layers on each side of the channel serve as electrodes (Fig. 3). The epitaxy of these cells accommodates (1×1)-CrI_3 on (2×2)-TMD layers. Equilibrium configurations for all TMD/CrI_3 heterojunctions are obtained by holding the in-plane lattice constant fixed to that of CrI_3 ($a = 6.79$ Å) while varying the out-of-plane lattice parameter. Assuming periodic boundary conditions in all three dimensions, systems are relaxed until atomic forces fall below 0.01 eV/Å.

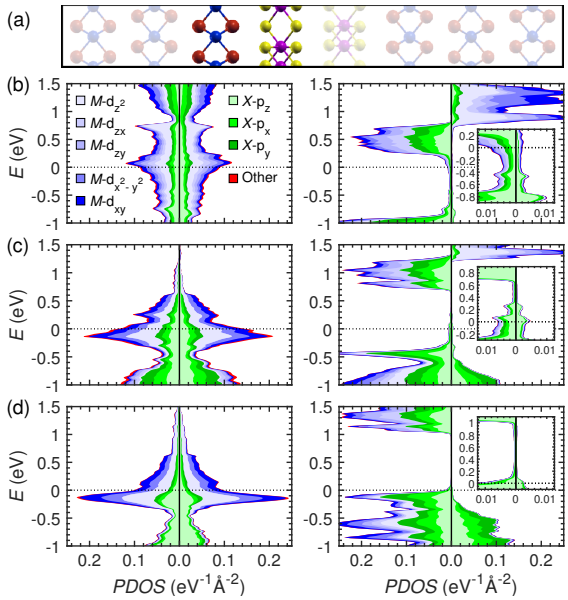

FIG. 3. (a) Schematic of a (2×2)-TMD/(1×1)-CrI_3 magnetic tunnel junction, where solid lines mark the supercell of the structure. Layer resolved PDOS for the 2L-CrI_3 channel and different metal electrodes (from top to bottom): (b) 1T-$TaSe_2$, (c) 2H-$NbSe_2$, and (d) 2H-TaS_2. Spin-resolved projections onto localized atomic orbitals on one of the CrI_3 layers and its adjacent TMD layer are plotted in the right and left column respectively.

To visualize the resulting TMD/2L-CrI_3 heterojunction band alignments, in Fig. 3 we compare the spin-resolved projected DOS (PDOS) of neighboring TMD and CrI_3. For 1T-$TaSe_2$ (low work function) electrodes, the Fermi level falls 0.2 eV below the spin majority CrI_3 CBE; for 2H-$NbSe_2$ and 2H-TaS_2 electrodes, Fermi energies reside 0.4 eV and 0.1 eV above the spin majority VBE of CrI_3, respectively. Owing to enhanced magnetic coupling in these systems, the spin majority FM CBE is nearly 0.1 eV below the AFM counterpart, while VBEs remain aligned [35, 38].

Spin polarization in the neighboring TMD layer is minor compared to that of the CrI_3 channel. Evinced in the layer resolved PDOS decomposition, the emergence of metal-induced gap states (MIGS) reveals non-negligible interlayer coupling between the electrode and

channel layers in the cases of 1T-$TaSe_2$ and 2H-$NbSe_2$ electrodes. Seen in the insets of Fig. 3, MIGS formed in MTJs with 1T-$TaSe_2$ electrodes extend through the entire band gap, comprised of mainly I p-orbitals followed by Cr d-orbitals. For 2H-$NbSe_2$ electrodes, these states primarily entail I p-orbitals and vanish in the upper half due to the low DOS in the adjacent TMD.

Next, transmissions T_s^m are obtained using coefficients $t_{i,j}^{s,m}(E, \mathbf{k}_\parallel)$ in Eq. 1 obtained employing the NEGF method implemented in the transportPAO code [46, 47], which offers a more accurate (and computationally demanding) characterization of transport. The transmissions for the 2L- and 4L-CrI_3 junctions in the FM and AFM configurations using a 36×36 $\mathbf{k}_\parallel$-mesh exhibit most of the features predicted from the CBS (Fig. 4): (*i*) large transmission values near the band edges; (*ii*) net transmissions drop roughly an order of magnitude per CrI_3 layer for carrier energies within the gap; and (*iii*) for FM cases, current contributions from spin minority modes at times surpass those of the spin majority.

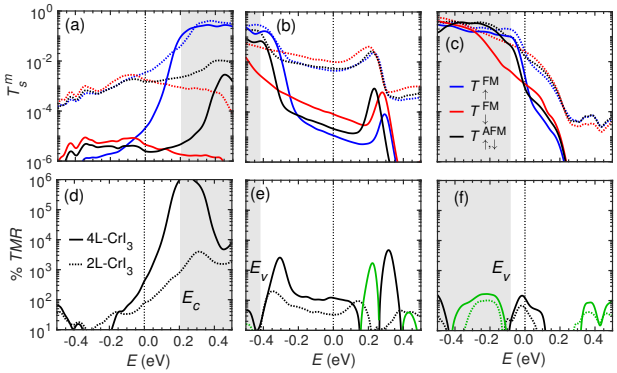

FIG. 4. Transmissions T_s^m (top) and corresponding TMR (bottom) for 2L- and 4L-thick CrI_3 MTJs with different electrodes: (a) 1T-$TaSe_2$, (b) 2H-$NaSe_2$, and (c) 2H-TaS_2. For the FM configuration we plot the spin majority (blue) and minority (red) contributions; while for the AFM configuration we average spin channels (black). Shaded areas denote CrI_3 spin majority band edges. Curves for bilayer (tetralayer) junctions are indicated by dotted (solid) lines. Black portions of the TMR curves denote $\sigma_{min} = \sigma_{\mathrm{AFM}}$ while green ones allude to $\sigma_{min} = \sigma_{\mathrm{FM}}$.

Around the Fermi level, heterostructures with 1T-$TaSe_2$ (low work function) electrodes produce spin majority transmissions in the FM configuration that dominate those of the spin minority or the AFM configuration [Fig. 4(a)], as expected from the CBS (Fig. 1). In contrast, differences between FM and AFM spin majority transmissions [Fig. 4(c)] dwindle with high work function leads (2H-$TaSe_2$) as the valence band edges align [38]. For 2H-$NbSe_2$ electrodes [Fig. 4(b)], spin transmissions that occur far from band edges are governed by the spin minority and present spikes at energies $\sim$0.25 eV above the Fermi level attributed to MIGS (Fig. 3) that effectively shorten the barrier thickness. Accounting for these interactions require full atomistic descriptions of the interfaces and cannot be anticipated from their bulk properties.

In 1T-$TaSe_2$/4L-CrI_3 junctions, TMR is twice that of graphite/2L-CrI_3 systems at similar conductivity levels while conductivities in thinner junctions (1T-$TaSe_2$/2L-CrI_3) increase by two orders of magnitude with only a small detriment to TMR [35]. Near the Fermi level, TMR values of $\sim$ 80% and $\sim$ 420% are achieved in 2L and 4L-CrI_3 systems, respectively (Fig. 4). Moreover, in agreement with CBS estimates, these values surge rapidly as carrier energies approach the CrI_3 CBE, a feature that may be accessed via electrostatic gating [8]. Similar results supporting these findings are also obtained for $NiTe_2$/$CrBr_3$ heterostructures [38]. For the 2H-$NbSe_2$ or 1T-TaS_2 leads, the TMR order of magnitude near the Fermi level is on par with results in junctions with graphite leads and CBS predictions. However, TMR results can deviate significantly from those predictions near the midgap and the VBE. These departures emerge due to the reduced filling factor ν for carrier energies moving into the gap [Fig. 2(c)], the presence of MIGS, and the similar FM and AFM decay rates near the VBE.

The applicability of our approach to 2D materials heterostructures stems from the weak interlayer coupling, allowing properties of the system to be decomposed in terms of their material constituents. An important consideration that ensures successful CBS predictions is a large electrode filling factor $\nu(E)$. CBS estimates face limitations when dominant contributions to transmissions originate from reduced regions of the BZ due to either strong coherence between electrodes and tunneling barriers [48] or the electronic dispersion of these layers [49, 50]. While full detailed calculations presented here are limited to those with hexagonal lattices, CBS estimates are expected to be valid in other crystal structures (e.g. 1T' and pcba). We thus anticipate that other low work function metals – such as 1T-VTe_2 [51], 1T-$NiTe_2$ [43], 1T'-$MoTe_2$ [52], 1T'-WTe_2 [53], or 1T'-$ReSe_2$ [54] – may also yield similar results.

In summary, enhanced conductivities and TMR in 2D materials heterostructures are demonstrated through barrier engineering. We predict TMR improvements using low work function TMD electrodes through spin injection near the CrI_3 conduction band edge. Away from the band edges, where evanescent modes decay more rapidly, results are susceptible to lead/channel interactions. Additionally, these systems offer up to three orders of magnitude greater conductivities than those with graphitic electrodes. The approach employed here enables the data-driven design of 2D material heterostructures and shows good agreement with the NEGF approach. The method is based on first principles calculations of bulk electrodes and channels, allowing computationally challenging descriptions of the electronic structure and transport of full heterostructures to be circumvented. By identifying candidate materials based on their bulk properties, our methodology may accelerate the guided design of devices based on the growing family of 2D materials, expanding the properties of advanced functional materi-

als.

ACKNOWLEDGMENTS

J.J.H. and M.A.K. are thankful for the support from the NSF-1848344 grant. The authors would also like to acknowledge the Auburn University Hopper and Easley HPC clusters for computational resources.

[1] A. K. Geim and I. V. Grigorieva, "Van der waals heterostructures," Nature **499**, 419–425 (2013).

[2] Yanping Liu, Siyu Zhang, Jun He, Zhiming M. Wang, and Zongwen Liu, "Recent progress in the fabrication, properties, and devices of heterostructures based on 2d materials," Nano-Micro Letters **11**, 13 (2019).

[3] D. R. Klein, D. MacNeill, J. L. Lado, D. Soriano, E. Navarro-Moratalla, K. Watanabe, T. Taniguchi, S. Manni, P. Canfield, J. Fernández-Rossier, and P. Jarillo-Herrero, "Probing magnetism in 2d van der waals crystalline insulators via electron tunneling," Science **360**, 1218–1222 (2018).

[4] Hyun Ho Kim, Bowen Yang, Shangjie Tian, Chenghe Li, Guo-Xing Miao, Hechang Lei, and Adam W Tsen, "Tailored tunnel magnetoresistance response in three ultrathin chromium trihalides," Nano letters **19**, 5739–5745 (2019).

[5] Tiancheng Song, Xinghan Cai, Matisse Wei-Yuan Tu, Xiaoou Zhang, Bevin Huang, Nathan P Wilson, Kyle L Seyler, Lin Zhu, Takashi Taniguchi, Kenji Watanabe, Michael A. McGuire, David H. Cobden, Di Xiao, Wang Yao, and Xiaodong Xu, "Giant tunneling magnetoresistance in spin-filter van der waals heterostructures," Science **360**, 1214–1218 (2018).

[6] Zhe Wang, Ignacio Gutiérrez-Lezama, Nicolas Ubrig, Martin Kroner, Marco Gibertini, Takashi Taniguchi, Kenji Watanabe, Ataç Imamoğlu, Enrico Giannini, and Alberto F Morpurgo, "Very large tunneling magnetoresistance in layered magnetic semiconductor cri3," Nature communications **9**, 1–8 (2018).

[7] Hyun Ho Kim, Bowen Yang, Tarun Patel, Francois Sfigakis, Chenghe Li, Shangjie Tian, Hechang Lei, and Adam W Tsen, "One million percent tunnel magnetoresistance in a magnetic van der waals heterostructure," Nano letters **18**, 4885–4890 (2018).

[8] Tiancheng Song, Matisse Wei-Yuan Tu, Caitlin Carnahan, Xinghan Cai, Takashi Taniguchi, Kenji Watanabe, Michael A McGuire, David H Cobden, Di Xiao, Wang Yao, and Xiaodong Xu, "Voltage control of a van der waals spin-filter magnetic tunnel junction," Nano letters **19**, 915–920 (2019).

[9] A. Manchon, J. Železný, I. M. Miron, T. Jungwirth, J. Sinova, A. Thiaville, K. Garello, and P. Gambardella, "Current-induced spin-orbit torques in ferromagnetic and antiferromagnetic systems," Rev. Mod. Phys. **91**, 035004 (2019).

[10] Kapildeb Dolui, Marko D. Petrović, Klaus Zollner, Petr Plecháč, Jaroslav Fabian, and Branislav K. Nikolić, "Proximity spin–orbit torque on a two-dimensional magnet within van der waals heterostructure: Current-driven antiferromagnet-to-ferromagnet reversible nonequilibrium phase transition in bilayer cri3," *Nano Letters*, Nano Letters **20**, 2288–2295 (2020).

[11] Lishu Zhang, Jun Zhou, Hui Li, Lei Shen, and Yuan Ping Feng, "Recent progress and challenges in magnetic tunnel junctions with 2d materials for spintronic applications," Applied Physics Reviews **8**, 021308 (2021), https://doi.org/10.1063/5.0032538.

[12] Tula R Paudel and Evgeny Y Tsymbal, "Spin filtering in cri3 tunnel junctions," ACS applied materials & interfaces **11**, 15781–15787 (2019).

[13] Jiaqi Zhou, Junfeng Qiao, Chun-Gang Duan, Arnaud Bournel, Kang L Wang, and Weisheng Zhao, "Large tunneling magnetoresistance in vse2/mos2 magnetic tunnel junction," ACS applied materials & interfaces **11**, 17647–17653 (2019).

[14] Lyudmila V Begunovich, Artem V Kuklin, Maxim A Visotin, Alexander A Kuzubov, Felix N Tomilin, Anton S Tarasov, Yuri G Mikhalev, and Pavel V Avramov, "Triple vte2/graphene/vte2 heterostructures as perspective magnetic tunnel junctions," Applied Surface Science **510**, 145315 (2020).

[15] Fangfang Li, Baishun Yang, Yu Zhu, Xiufeng Han, and Yu Yan, "Four distinct resistive states in van der waals full magnetic 1t-vse2/cri3/1t-vse2 tunnel junction," Applied Surface Science **505**, 144648 (2020).

[16] Miho Arai, Rai Moriya, Naoto Yabuki, Satoru Masubuchi, Keiji Ueno, and Tomoki Machida, "Construction of van der waals magnetic tunnel junction using ferromagnetic layered dichalcogenide," Applied Physics Letters **107**, 103107 (2015).

[17] Weiyi Wang, Awadhesh Narayan, Lei Tang, Kapildeb Dolui, Yanwen Liu, Xiang Yuan, Yibo Jin, Yizheng Wu, Ivan Rungger, Stefano Sanvito, and Faxian Xiu, "Spin-valve effect in nife/mos2/nife junctions," Nano letters **15**, 5261–5267 (2015).

[18] Kangkang Zhao, Yanhui Xing, Jun Han, Jiafeng Feng, Wenhua Shi, Baoshun Zhang, and Zhongming Zeng, "Magnetic transport property of nife/wse2/nife spin valve structure," Journal of Magnetism and Magnetic Materials **432**, 10–13 (2017).

[19] Muhammad Farooq Khan, Hakseong Kim, Ghazanfar Nazir, Suyong Jung, and Jonghwa Eom, "Layer dependent magnetoresistance of vertical mos 2 magnetic tunnel junctions," Nanoscale **10**, 16703–16710 (2018).

[20] Xinlu Li, Jing-Tao Lü, Jia Zhang, Long You, Yurong Su, and Evgeny Y. Tsymbal, "Spin-dependent transport in van der waals magnetic tunnel junctions with fe3gete2 electrodes," *Nano Letters*, Nano Letters **19**, 5133–5139 (2019).

[21] Pradeep Kumar, Anuj Kumar, and Davinder Kaur, "Spin valve effect in sputtered fl-mos2 and ferromagnetic shape memory alloy based magnetic tunnel junction," Ceramics International **47**, 4587–4594 (2021).

[22] John P. Perdew, Kieron Burke, and Matthias Ernzerhof, "Generalized gradient approximation made simple," Phys. Rev. Lett. **78**, 1396–1396 (1997).

[23] M. Dion, H. Rydberg, E. Schröder, D. C. Langreth, and B. I. Lundqvist, "Van der waals density functional for general geometries," Phys. Rev. Lett. **92**, 246401 (2004).

[24] T. Thonhauser, Valentino R. Cooper, Shen Li, Aaron Puzder, Per Hyldgaard, and David C. Langreth, "Van der waals density functional: Self-consistent potential and the nature of the van der waals bond," Phys. Rev. B **76**, 125112– (2007).

[25] Valentino R. Cooper, "Van der waals density functional: An appropriate exchange functional," Phys. Rev. B **81**, 161104 (2010).

[26] P. E. Blöchl, "Projector augmented-wave method," Phys. Rev. B **50**, 17953–17979 (1994).

[27] Andrea Dal Corso, "Pseudopotentials periodic table: From h to pu," Comput. Mater. Sci. **95**, 337 – 350 (2014).

[28] Hendrik J. Monkhorst and James D. Pack, "Special points for brillouin-zone integrations," Phys. Rev. B **13**, 5188–5192 (1976).

[29] Paolo Giannozzi, Oliviero Andreussi, Thomas Brumme, Oana Bunau, M Buongiorno Nardelli, Matteo Calandra, Roberto Car, Carlo Cavazzoni, Davide Ceresoli, Matteo Cococcioni, N Colonna, I Carnimeo, A Dal Corso, S de Gironcoli, P Delugas, R. A. DiStasio Jr., A Ferretti, A Floris, G Fratesi, G Fugallo, R Gebauer, U Gerstmann, F Giustino, T Gorni, J Jia, M Kawamura, H.-Y. Ko, A Kokalj, E Kucukbenli, M Lazzeri, M Marsili, N Marzari, F Mauri, N. L. Nguyen, H.-V. Nguyen, A Otero-de-la Roza, L Paulatto, S Ponce', D Rocca, R Sabatini, B Santra, M Schlipf, A. P. Seitsonen, A Smogunov, I Timrov, T Thonhauser, P Umari, N Vast, X Wu, and S Baroni, "Advanced capabilities for materials modelling with quantum espresso," Journal of Physics: Condensed Matter **29**, 465901 (2017).

[30] Alexander Smogunov, Andrea Dal Corso, and Erio Tosatti, "Ballistic conductance of magnetic co and ni nanowires with ultrasoft pseudopotentials," Phys. Rev. B **70**, 045417 (2004).

[31] Matthew G Reuter, "A unified perspective of complex band structure: interpretations, formulations, and applications," Journal of Physics: Condensed Matter **29**, 053001 (2016).

[32] Adam M. Pfeifle and Marcelo A. Kuroda, "Tunable contact resistance in transition metal dichalcogenide lateral heterojunctions," Phys. Rev. Materials **4**, 024002 (2020).

[33] Supriyo Datta, *Electronic Transport in Mesoscopic Systems*, Cambridge Studies in Semiconductor Physics and Microelectronic Engineering (Cambridge University Press, Cambridge, 1995).

[34] Aldo Di Carlo, P. Vogl, and W. Pötz, "Theory of zener tunneling and wannier-stark states in semiconductors," Phys. Rev. B **50**, 8358–8377 (1994).

[35] Jonathan J Heath, Marcio Costa, Marco Buongiorno-Nardelli, and Marcelo A Kuroda, "Role of quantum confinement and interlayer coupling in cri3-graphene magnetic tunnel junctions," Physical Review B **101**, 195439 (2020).

[36] Qing Hua Wang, Kourosh Kalantar-Zadeh, Andras Kis, Jonathan N Coleman, and Michael S Strano, "Electronics and optoelectronics of two-dimensional transition metal dichalcogenides," Nature nanotechnology **7**, 699–712 (2012).

[37] Stefano Curtarolo, Wahyu Setyawan, Gus LW Hart, Michal Jahnatek, Roman V Chepulskii, Richard H Taylor, Shidong Wang, Junkai Xue, Kesong Yang, Ohad Levy, Michael J. Mehl, Harold T. Stokes, Denis O. Demchenko, and Dane Morgan, "Aflow: An automatic framework for high-throughput materials discovery," Computational Materials Science **58**, 218–226 (2012).

[38] See Supplemental Material at [URL will be inserted by publisher] for TMD electrode prioritization, geometric properties of TMD/CrX_3 structures, and $NiTe_2$/$CrBr_3$ performance.

[39] M Marezio, PD Dernier, A Menth, and GW Hull Jr, "The crystal structure of nbse2 at 15 k," Journal of Solid State Chemistry **4**, 425–429 (1972).

[40] David Eugene Moncton, JD Axe, and FJ DiSalvo, "Neutron scattering study of the charge-density wave transitions in 2h-ta se2 and 2h-nbse2," Physical Review B **16**, 801 (1977).

[41] Gerrit A Wiegers, Jan L de Boer, Auke Meetsma, and Sander van Smaalen, "Domain structure and refinement of the triclinic superstructure of 1t-tase2 by single crystal x-ray diffraction," Zeitschrift für Kristallographie-Crystalline Materials **216**, 45–50 (2001).

[42] A Meetsma, GA Wiegers, RJ Haange, and JL De Boer, "Structure of 2h-tas2," Acta Crystallographica Section C: Crystal Structure Communications **46**, 1598–1599 (1990).

[43] Chunqiang Xu, Bin Li, Wenhe Jiao, Wei Zhou, Bin Qian, Raman Sankar, Nikolai D Zhigadlo, Yanpeng Qi, Dong Qian, Fang-Cheng Chou, and Xiaofeng Xu, "Topological type-ii dirac fermions approaching the fermi level in a transition metal dichalcogenide nite2," Chemistry of materials **30**, 4823–4830 (2018).

[44] FJ Di Salvo, RG Maines, JV Waszczak, and RE Schwall, "Preparation and properties of 1t-tase2," Solid State Communications **14**, 497–501 (1974).

[45] FR Gamble, Jeanne H Osiecki, and FJ DiSalvo, "Some superconducting intercalation complexes of tas2 and substituted pyridines," The Journal of Chemical Physics **55**, 3525–3530 (1971).

[46] Marco Buongiorno Nardelli, "Electronic transport in extended systems: Application to carbon nanotubes," Phys. Rev. B **60**, 7828–7833 (1999).

[47] Marco Buongiorno Nardelli, Frank T. Cerasoli, Marcio Costa, Stefano Curtarolo, Riccardo De Gennaro, Marco Fornari, Laalitha Liyanage, Andrew R. Supka, and Haihang Wang, "Paoflow: A utility to construct and operate on ab initio hamiltonians from the projections of electronic wavefunctions on atomic orbital bases, including characterization of topological materials," Comput. Mater. Sci. **143**, 462–472 (2018).

[48] W. H. Butler, X.-G. Zhang, T. C. Schulthess, and J. M. MacLaren, "Spin-dependent tunneling conductance of Fe|MgO|Fe sandwiches," Phys. Rev. B **63**, 054416 (2001).

[49] V. M. Karpan, G. Giovannetti, P. A. Khomyakov, M. Talanana, A. A. Starikov, M. Zwierzycki, J. van den Brink, G. Brocks, and P. J. Kelly, "Graphite and graphene as perfect spin filters," Phys. Rev. Lett. **99**, 176602 (2007).

[50] Marcelo A. Kuroda, J. Tersoff, Dennis M. Newns, and Glenn J. Martyna, "Conductance through multilayer graphene films," Nano Lett. **11**, 3629–3633 (2011).

[51] Xingyuan Ma, Tian Dai, Shuai Dang, Songdan Kang, Xuexian Chen, Wenqi Zhou, Gaili Wang, Hongwei Li, Ping Hu, Zhihao He, Yue Sun, Dan Li, Fengmei Yu, Xi-

ang Zhou, Huanjun Chen, Xinman Chen, Shuxiang Wu, and Shuwei Li, "Charge density wave phase transitions in large-scale few-layer 1t-vte2 grown by molecular beam epitaxy," *ACS Applied Materials & Interfaces*, ACS Applied Materials & Interfaces **11**, 10729–10735 (2019).

[52] Carl H. Naylor, William M. Parkin, Jinglei Ping, Zhaoli Gao, Yu Ren Zhou, Youngkuk Kim, Frank Streller, Robert W. Carpick, Andrew M. Rappe, Marija Drndić, James M. Kikkawa, and A. T. Charlie Johnson, "Monolayer single-crystal 1t'-mote2 grown by chemical vapor deposition exhibits weak antilocalization effect," *Nano Letters*, Nano Letters **16**, 4297–4304 (2016).

[53] Michal J. Mleczko, Runjie Lily Xu, Kye Okabe, Hsueh-Hui Kuo, Ian R. Fisher, H.-S. Philip Wong, Yoshio Nishi, and Eric Pop, "High Current Density and Low Thermal Conductivity of Atomically Thin Semimetallic WTe2," ACS Nano **10**, 7507–7514 (2016).

[54] Amey Apte, Aravind Krishnamoorthy, Jordan A. Hachtel, Sandhya Susarla, Jongwon Yoon, Lucas M. Sassi, Palash Bharadwaj, James M. Tour, Juan Carlos Idrobo, Rajiv K. Kalia, Aiichiro Nakano, Priya Vashishta, Chandra Sekhar Tiwary, and Pulickel M. Ajayan, "Two-dimensional lateral epitaxy of 2h(mose2)–1t'(rese2) phases," *Nano Letters*, Nano Letters **19**, 6338–6345 (2019).